Research Article | Vol. 30, No. 8 / 11 Apr 2022 / Optics Express 12237

Optics EXPRESS

Aspherical liquid crystal lenses based on a variable transmission electrode

N. BENNIS,[1] T. JANKOWSKI,[2] P. MORAWIAK,[1] A. SPADLO,[1] D. C. ZOGRAFOPOULOS,[3] J. M. SÁNCHEZ-PENA,[4] J. M. LÓPEZ-HIGUERA,[5,6,7] AND J. F. ALGORRI[5,6,7,*]

[1]*Faculty of Advanced Technologies and Chemistry, Military University of Technology, Warsaw 00-908, Poland*
[2]*Faculty of Mechatronics, Warsaw University of Technology, Św. Andrzeja Boboli 8, 02-525 Warsaw, Poland*
[3]*Consiglio Nazionale delle Ricerche, Istituto per la Microelettronica e Microsistemi (CNR-IMM), Roma 00133, Italy*
[4]*Department of Electronic Technology, Carlos III University, Madrid 28911, Spain*
[5]*Photonics Engineering Group, University of Cantabria, 39005 Santander, Spain*
[6]*CIBER-bbn, Instituto de Salud Carlos III, 28029 Madrid, Spain*
[7]*Instituto de Investigación Sanitaria Valdecilla (IDIVAL), 39011 Santander, Spain*
[*]*algorrijf@unican.es*

Abstract: In this work, a technique to generate aspherical liquid crystal lenses with positive and negative optical power is experimentally demonstrated. The main enabling element is a micro-metric electrode with variable spatial size. This produces a decreasing resistance towards the lens centre that generates the desired voltage/phase profiles. Then, the voltage is homogeneously distributed across the active area of the lens by micro-metric concentric electrodes. As it is demonstrated, the phase shift can be controlled with voltages from 0 to 4.5 V_{RMS}. As a result, parabolic profiles are obtained both for negative and positive optical powers. Furthermore, this approach avoids some disadvantages of previous techniques; parabolic profiles can be obtained with only one lithographic step and one or two voltage sources. Other complex aspherical profiles could be fabricated using the same technique, such as elliptical or hyperbolic ones.

© 2022 Optica Publishing Group under the terms of the Optica Open Access Publishing Agreement

1. Introduction

Liquid crystals (LC) are exploited in numerous applications beyond their traditional use in displays. For example, they have been proposed as sensors [1,2], in optical communications [3], astronomy [4,5] or plasmonics [6,7]. Among all of these non-display applications, LC phase modulators have attracted significant attention [8]. Today this is still a hot research topic, e.g., for the correction of aberrations [9], ophthalmological applications [10], tunable zooming [11], beam steering [12], 3D vision devices [13,14], optical vortices [15–17], etc. Among all such applications, adaptive-focus lenses are one of the most important. First structures were proposed in the late 1970s by Berreman *et al.* (with patent application in 1977 [18]) and Sato *et al.* in 1979 [19]. These structures were based on a curved cavity that was filled with LC. One of the main problems was the long response time due to the increased LC layer thickness. In addition, the molecular orientation suffered from inhomogeneity.

Following that, the first demonstration of a cylindrical LC lens was performed in 1981 [20]. In that case, the voltage gradient was achieved through several electrodes. The use of multiple electrodes has been employed until now [21–24] to solve the problem of producing large-aperture lenses. However, the use of a large number of independently controlled electrodes faces the issues of complex fabrication process and, particularly, complex driving circuits for voltage control.

#451292 https://doi.org/10.1364/OE.451292
Journal © 2022 Received 14 Dec 2021; revised 1 Mar 2022; accepted 1 Mar 2022; published 28 Mar 2022

Optics EXPRESS

A solution to solve these drawbacks was proposed in the 80s by A.F. Naumov *et al.* [25]. By using a high resistivity layer, the strong voltage drop at the lens centre was avoided [26]. The sheet resistance of the control electrode was a key design parameter. The larger the diameter, the lower the sheet resistance; typical values are in the order of 100 kΩ/sq to a few MΩ/sq for lens diameters in the order of millimetres [27]. Although this approach greatly alleviates the problem of complex voltage control (only one or two sources are required), the fabrication process requires the deposition of very thin layers. Nevertheless, in recent years several research groups have worked on this technique [28–31] and some companies have used them in cell phone cameras (e.g. Karbonn) and webcams (e.g. Creative Labs) [32,33].

Over the last years, several structures have been proposed to address the aforementioned problems [34,35]. Despite this, complex fabrication processes, multiple electrodes or high voltage control are still present in most of them. Recently, we proposed a novel structure that is capable of distributing the voltage across the lens aperture by using only one lithographic step in the fabrication process and only one or two voltage sources [36]. Furthermore, based on the same technique, other devices, such as Powell lenses or beam steerers have been proposed [37,38]. The main problem of these devices is that voltage drop from the lens periphery to the centre is based on a rectangular transmission electrode, causing a linear voltage drop. The resulting phase profiles are suitable for axicon and Powell lenses, which can be slightly curved if the birefringence curve is appropriately compensated by proper voltage selection. Despite this, the design of nonlinear phase profiles is difficult and strongly depending on the LC electro-optical characteristics. To solve this problem, it has been theoretically proposed that a modification in the transmission electrode shape is capable of producing aspherical profiles [39].

Any lens with surfaces that are not portion of a sphere can be considered aspherical. In this type of lens, the radius of curvature changes with distance from the optical axis (unlike a sphere that has a constant radius). Thanks to their shape, aspheric lenses deliver improved optical performance compared to standard spherical surfaces. They have long been known to effectively correct various types of lens aberrations, such as those produced in optical design or spherical lenses. Despite this, they are difficult to fabricate with precision and are usually used in professional-level optics. For this reason, aspherical lenses with tunable optical power will be highly demanded in some emerging applications, such as in virtual and augmented reality, to reduce distortion in the lens centre (e.g. PS VR [40]) and solve the Accommodation-Convergence (AC) mismatch issue with better optical quality than spherical lenses [41,42]. Aspherical lenses are usually described by the surface profile (sag) given by Eq. (1) [43]:

$$z(h) = \frac{ch^2}{1 + \sqrt{1 - (1 + k)c^2h^2}} + A_4h^4 + A_6h^6 + A_8h^8 + \ldots, \tag{1}$$

where z is the sag of the surface parallel to the optical axis, h is the radial distance from the optical axis, c is the curvature inverse of radius, k is the conic constant, A_{2n}, $n>1$ are the $2n$-th orders of aspheric coefficients (terms that allow for higher-order aspheric optical elements to be defined). When the aspheric coefficients are equal to zero, the resulting aspheric surface is considered to be a conic. Depending on the k-constant the conic surface can be an hyperbola (k < -1), a parabola (k = -1) and a prolate ellipse (-1 < k < 0). If the k-factor is equal to zero the surface is spherical and values higher than 0 produce oblate ellipses [43].

This work proposes a trapezoidal-shaped transmission electrode to generate tunable aspherical phase profiles. As proof of concept, we have designed the transmission electrode to generate aspherical lenses with k = -1 (parabolic profiles), following the design principles demonstrated in Ref. [39]. The Transmission Electrode LC Lens (TELCL) is experimentally demonstrated by measuring fringe patterns through crossed-polarisers, the resulting phase profiles, optical power and aberrations. This experimental verification of the proof-of-concept may open the path to optimized the design of aspherical tunable lens with simple microfabrication techniques.

Optics EXPRESS

2. Operating principle and fabrication

The structure consists of a transmission electrode, acting as a distributed voltage divider, shown in Fig. 1(a), and an array of concentric electrode stubs evenly arranged, which distribute homogeneously the voltage across the lens aperture, as in Fig. 1(b), marked with red colour. As it can be observed in Fig. 1(a), the transmission electrode consists of two parts, a trapezoidal-shaped electrode, which has a decreasing resistance towards the lens centre [Fig. 1(a): R_1], and a rectangular electrode with homogeneously distributed resistance [Fig. 1(a): R_2]. The variable electrode R_1 is the key component of this structure, as it produces a nonlinear voltage drop from the side to the lens centre. On the other hand, the concentric electrodes behave like the high resistivity layer of a modal device, but with the advantage of being made by a simple lithographic process with low resistivity materials, such as commercial indium-tin oxide (ITO). In addition, there is a circular patch at the lens centre to flatten the curve at this region (the size has to be optimised as a function of the desired aspherical profile). The gap between electrodes g is not an issue, considering standard photolithography resolutions (in the order of a few microns) [36]. It is stressed that the concentric electrodes distribute the voltage profile of the electrode R_1, which varies from V_1 to V_c according to Fig. 1(b). The electrode R_2 serves to address laterally the tunable lens with the voltage signal V_2 in order to adjust the voltage V_c at the lens centre.

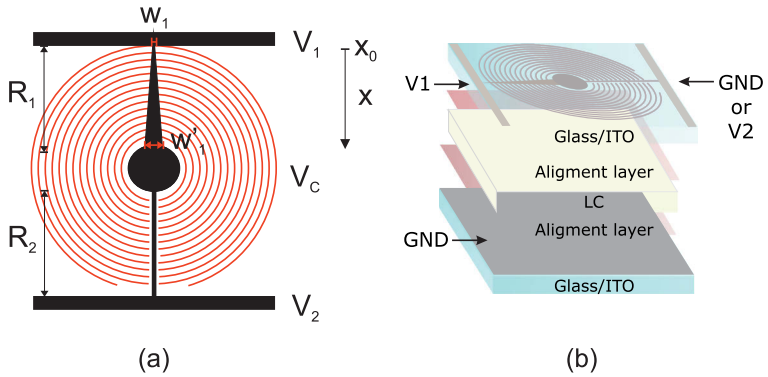

Fig. 1. (a) Schematic depiction of the electrode structure for the distribution of the voltage signals. Transmission electrode (black) and concentric stubs that distribute homogeneously the voltage profile across the entire surface (red). Note that the stub electrodes are in contact only with the electrode R_1 and therefore they distribute the $V(x)$ profile of the trapezoidal-shaped electrode R_1. (b) Schematic depiction of the TELCL arrangement.

The voltage distribution between V_1 to V_c can be deduced from Ohm's law and is given by Eq. (2) [39] (it can be considered $x = 0$ at V_1 and x towards V_c)

$$V(x) = V_1 + (V_c - V_1)\frac{\ln\left(\frac{w_1 + mx}{w_1}\right)}{\ln\left(\frac{w_1'}{w_1}\right)}, \tag{2}$$

where m is the slope of the variable electrode that depends on the difference between w_1 and w_1' and the electrode length L:

$$m = \frac{w_1' - w_1}{L}. \tag{3}$$

We have used commercially available glass for the fabrication, covered by a conducting ITO layer. These glass substrates can be distinguished by three properties: glass thickness, ITO

Optics EXPRESS

thickness/resistivity and flatness. Flatness and resistivity are the most important issues from our point of view. A Glaston polished glass (supertwist quality) with a thickness of 0.7 mm and a 125 nm layer of ITO is used to manufacture the proposed devices. The ITO layer is almost transparent (80-90%) with a surface resistivity of 100 Ω/sq. The substrates are cleaned in two stages of the manufacturing process: after cutting the substrate and immediately after the photolithographic process. First, substrates are cleaned with acetone and isopropyl alcohol. Next, the substrates are submerged in ultrasonic bath with micro-filtered detergent during 20 min at 40°C. Finally, the glasses are rinsed in distilled flowing water during several minutes and dried with a nitrogen gun. To eliminate any portion of water that could be adsorbed in the glass or ITO layer, substrates are dried in the oven at 150°C for one hour.

For the photolithography process, the photoresist Microposit S1818 was employed. The photoresist was diluted in microposit solvent for high-resolution samples to achieve high resolution. Photoresist spin coating was made @4500 rpm, during 30 sec with an initial short ramp of 3 sec. For high resolution photolithographic process (less than 10 µm) concentrations 2:1 or 1:1 were used. The photoresist was cured in a conventional oven during 30 min @90°C (to evaporate the solvent) and another 30 min at 110°C. Isolation was made @4 mW/cm^2 during 4 sec for chromium-glass masks. The time is not critical for the developing process and varies from 70 for the thinnest layers to 120 sec for the thickest ones. After the developing process, substrates were baked again for 30 min @110°C to harden the photoresist. After the post-baking process, acid etching was made in a solution of 50% water, 49% hydrochloric acid solved @37% and 1% nitric acid. ITO etching was made @65°C for 35 sec.

The ITO coated glass substrates were spin coated at 4000 rpm for 40 sec with homogeneous alignment polyamide SE-130 (Nissan Chemical Industries, Ltd), prebaked on hot plate at 100°C for 10 min and finally backed in an oven at 210°C for 40 min. The polyimide on the substrate was rubbed in the direction of the electrodes for the upper substrate and an antiparallel direction for the other one. Finally, the nematic LC 6CHBT infiltrated the cavity, whose optical parameters are $n_e = 1.68$, $n_o = 1.52$ and $\Delta n = 0.16$ [44]. The thickness of the LC planar cell is 80 µm. The final dimensions are: $g = 10$ µm, $w_2 = 60$ µm, $w_1 = 10$ µm and $w_1' = 100$ µm. The circular patch at the lens centre has a diameter of 720 µm. The total diameter is 1 cm.

3. Setup and experimental results

The schematic of the optical system for measuring simultaneously the fringe patterns and optical power of the transmission electrode LC lens (TELCL) is shown in Fig. 2(a). A spatially filtered and collimated He-Ne laser (wavelength of 632.8 nm) impinges normally, after passing through the polariser, on the TELCL. A non-polarizing beam splitter (NPBS) is inserted after the TELCL to split the beam into two arms. The beam transmitted through the NBPS is focused by the TELCL on the CMOS2 camera. In this arm, a Shark-Hartmann (SH) sensor is used to obtain the curvature of transmitted beam by TELCL before and after the focal point. The negative radius of curvature, as in Fig. 2(c) represents divergent spherical wavefronts where the focused point is located in front of the sensor plane. In contrast, a positive curvature [Fig. 2(d)] indicates a convergent spherical wavefront with a virtual focal point behind the wavefront sensor reference plane.

This arm is employed to measure the effect of the TELCL on the deflection of the impinging laser beam. For this, a linearly polarized laser whose polarization is parallel to the LC molecular alignment is used. The Point Spread Function (PSF) is acquired by a second CMOS (CMOS 2). In the case of negative lenses, they create a virtual image that cannot be made visible on the screen. We can calculate their focal by placing a positive L4 lens at a small distance to the negative TELCL, as shown in the setup of Fig. 2(b). By combining a converging lens with a divergent lens, real images are generated. The formula for thin lenses, with a known power of

Optics EXPRESS

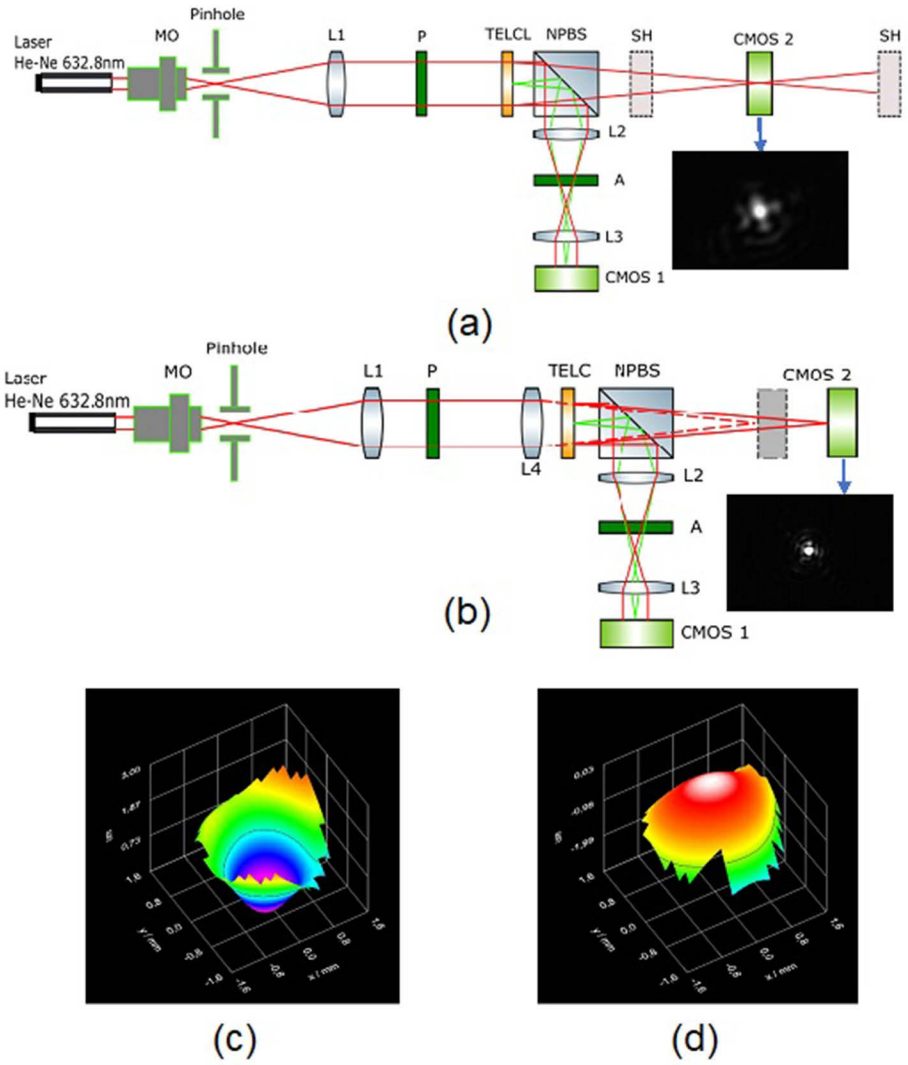

Fig. 2. Optical characterization of positive lens: (a) Schematic of the optical system for measuring simultaneously the fringe patterns and positive optical power of the TELCL. (b) Optical characterization setup for negative optical power lenses. (c) Convergent and (d) divergent spherical wavefront.

the converging lens, can be used to determine the power of the diverging lens. Most important condition: the two lens setup is positive (negative focal is larger than positive).

The reflected beam arm is used to evaluate the fringe pattern modulation across the TELCL placed between crossed polarized with its rubbing direction at 45° to the axis of polarization of the entrance beam. The image of the interference pattern is resized by two biconvex lenses (L2 and L3) and captured by the CMOS 1 camera, as shown in Fig. 2(a,b). The optical interference fringes were used to estimate the phase retardation profile of the lens. Light passing through areas accumulating a phase shift that is an odd multiple of π go through and produce maximum transmittance, whereas phase shift that is even multiple of π do not pass through and produce minimum transmittance. Therefore, the measurement of consecutive rings (maximum-minimum transmittance) gives the phase profile in steps of π.

Optics EXPRESS

As commented above, the variable transmission electrode produces a nonlinear voltage distribution, in accordance with Eq. (2). Then, the concentric electrodes distribute the voltage across the active area homogeneously. The measured total resistance between electrode V_1 and V_2 is 50 kΩ, mainly attributed to R_2. With this value, the expected current is in the order of μA. The experimental resistance is higher than the theoretical estimation, probably caused by an increase of the sheet resistance and a reduction of w_1 and w_1' in the acid attack. The voltages V_1 and V_2 were tested to obtain the most parabolic profiles possible, the values can be found in the caption of Fig. 3. The obtained interference patterns corresponding to +9, +7, +5, +3, −9, −7, −5, −3 ($\times 2\pi$ rad) are shown in Fig. 3 from (a) to (h), respectively. As can be seen in Fig. 3, the phase distribution is continuous, without any inhomogeneity (except for a small number of missing concentric electrodes). This indicates that the gap between concentric electrodes is not affecting the optical phase response. It has to be noted that this distance is only 10 μm whereas the LC thickness is around 80 μm. The experimental phase profiles of Fig. 4(a) are extracted by taking a diagonal line crossing the lens centre. Each ring is represented by a point indicating steps of π. When the voltage $V_1 > V_2$ positive lenses are obtained and vice versa.

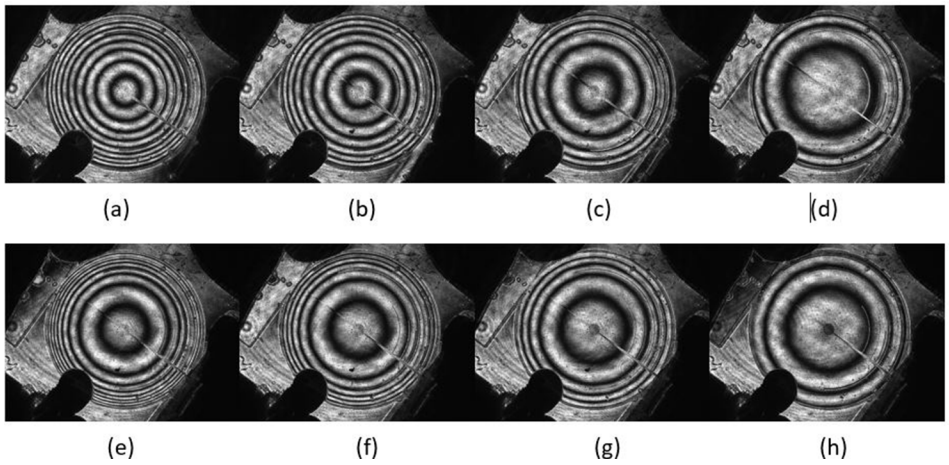

Fig. 3. Experimental optical phase shift produced by the proposed device for several voltages. Positive lens (V_{RMS} values): (a) V_1=1.85, V_2=0.6, (b) V_1=1.85, V_2=0.95, (c) V_1=1.85, V_2=1.25, (d) V_1=1.85, V_2=1.55. Negative lens (V_{RMS} values): (e) V_1=1.4, V_2=4.5, (f) V_1=1.6, V_2=4.5, (g) V_1=1.8, V_2=4.5, (h) V_1=2.1, V_2=4.5.

In Fig. 4(a) the dashed lines are the fitting curve of experimental data to Eq. (1). The phase profiles follow almost parabolic profiles for the positive lens with high optical power. The phase profiles for low optical power also have parabolic profiles for the negative lens, but for high optical power (e.g. $-9 \times 2\pi$) they show some aberrations. This can be caused by some mission concentric electrodes changing the expected voltage distribution in the transmission electrode. Nevertheless, it can be concluded that the lens is capable of producing positive and negative phase profiles with a good approximation to parabolic ones. More details about asphericity are included below. In Fig. 4(b) some simulations are shown, performed by using Frank-Oseen equations for the voltage-dependent switching in the LC cell [45] and Eqs. (2)–(3), taken into account the experimental voltages used in Fig. 3 and a LC cell thickness of 75 μm. Despite the overall agreement, there are some differences in the absolute phase values in some profiles. Some missing concentric electrodes could cause these differences (see Fig. 3), causing different voltage distributions than theoretical approximations, or not perfect alignment of the LC in the relatively thick employed cell, which could lead to a different LC effective birefringence curve. The photolithographic fabrication of the microelectrodes can be further optimized, or

Optics EXPRESS

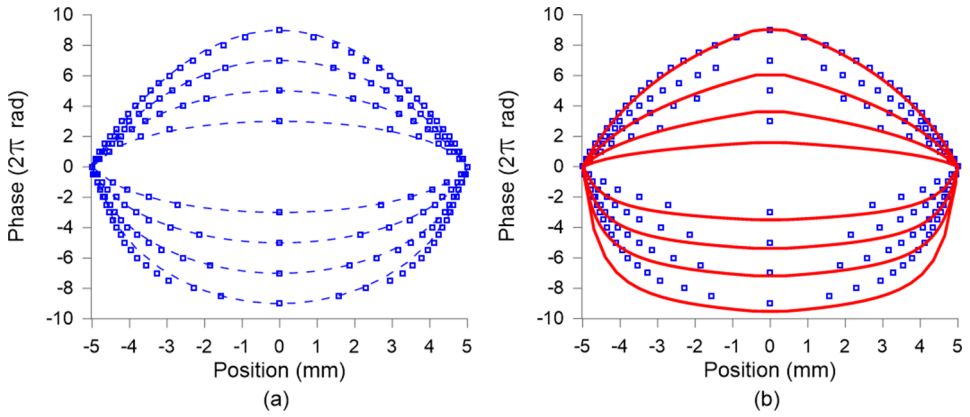

Fig. 4. Optical phase shift was generated by the proposed device for several voltages. (a) Experimental phase shift extracted from fringe patterns of Fig. 3 (points are experimental measurements and the line a fitting to Eq. (1)). (b) Simulations considering the voltages of Fig. 3 (points are experimental measurements and lines theoretical calculations).

alternatively, other techniques can be explored, such as laser ablation. It is stressed that this is the first proof-of-concept experimental demonstration of tunable LC lenses with parabolic phase profile based on the transmission electrode technique. From these results the focal length can be obtained. As can be observed in Fig. 5(a), the maximum optical power is 0.5 Dioptres (1/f). This value is low due to the LC birefringence. The graph of Fig. 5 (b) shows the Root-Mean-Square Error (RMSE) of Fig. 4(a), which is the square root of the average of squared errors (between Eq. (1) and experimental data). It can be observed that whereas the positive lens (dashed blue line) has a stable error around 0.28π rads from $V_2 = 0.4$ to 0.8 V_{RMS} (and 0.04π beyond this value), the negative lens (dashed red line) has an increasing error as the lens increases the optical power (from 0.02π to 0.8π). This effect can be seen in Fig. 4(a), where for the negative profiles the curve fitting is not optimum (it has to be taken into account that higher-order aspheric coefficients are not considered). Regarding the asphericity, the value of k is estimated by the curve fitting of Eq. (1) to the experimental data. Figure 5(b) shows this parameter's variation as a function of the optical power. In the case of the positive lens (solid blue line), the value of k = -1 from $V_2 = 0.4$ to 0.8 V_{RMS}. This indicates a perfect parabolic phase profile. Then, for higher voltages the phase profile resembles an elliptical profile. Something similar happens with the negative lens (solid red line), but in this case, it never reaches the parabolic profile, as the applied voltage for higher optical power is far from optimal. This effect can be considerably improved by using a theoretical model that allows us to estimate the exact voltages required to use the proper section of the LC effective birefringence curve. Moreover, as it is commented in [39], the pyramid-shaped electrodes have the best response for high phase shift modulation, but a considerable reduction of the fitting quality as the phase shift is reduced. One solution could be the use of parabola-shaped electrodes, which, as it has been theoretically demonstrated, have a more stable response to phase shift changes (tunability).

Thanks to the SH, the Zernike coefficients are extracted for the positive profiles of Fig. 4 (Table 1). Although the lens is not optimum because of the sub-optimal applied voltages and relatively large thickness, the measured aberration coefficients are generally low compared to other LC lenses [46]. Some effects can be explained following the same physical effects reported in the previous reference. These values can be reduced by optimising the applied voltages.

In addition, the image performance obtained by using the TELCL is demonstrated in Fig. 6. A piece of paper with letters is placed in front of the TELCL. The black circle indicates the active area (1 cm of diameter) At a starting point, in Fig. 6(c) the voltage is switched off. When the

Optics EXPRESS

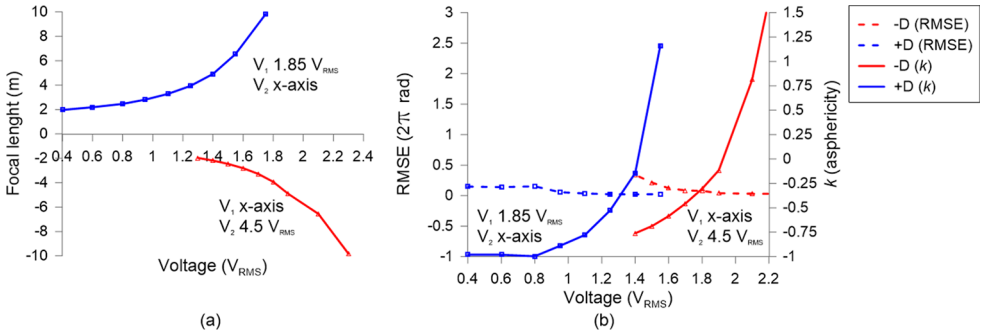

Fig. 5. (a) Focal length for different applied voltages. (b) RMSE (dashed line) and asphericity (solid line) of Fig.4 (a). Blue line positive lens (+D), red line negative lens (-D).

Table 1. Zernike coefitients (μm) for positive phase profiles.

Aberration	9 (2π) rad	7 (2π) rad	5 (2π) rad	3 (2π) rad
Piston	-0.199	-0.146	-0.096	-0.029
Tilt Y	0.012	0.049	0.085	0.099
Tilt X	-0.096	-0.146	-0.165	-0.155
Oblique astigmatism	-0.128	-0.154	-0.169	-0.164
Defocus	0.313	0.254	0.197	0.138
Vertical astigmatism	0.031	0.039	0.031	0.02
Vertical trefoil	-0.005	-0.001	-0.005	-0.01
Vertical coma	-0.01	-0.037	-0.059	-0.065
Horizontal coma	0.067	0.1	0.121	0.108
Oblique trefoil	-0.007	-0.005	-0.002	-0.002
Oblique quadrafoil	-0.005	-0.005	-0.005	-0.005
Oblique secondary astigmatism	0.004	0.005	-0.009	-0.019
Primary spherical	0.032	0.051	0.068	0.069
Vertical secondary astigmatism	-0.004	0.001	0.011	0.012
Vertical quadrafoil	-0.005	-0.006	-0.003	0.002

set of voltages V_1= 1.4 V_{RMS} and V_2 = 4.5 V_{RMS} is applied (negative lens), the image is out focus in Fig. 6(b), but when the objective focus is adjusted, it can be seen how the letters are reduced in size. In the same manner, if the applied voltage is V_1= 1.85 V_{RMS} and V_2 = 0.6 V_{RMS} (positive lens), in Fig. 6(e) the letters are increased in size. These results show that the effect of aberrations and scattering is considerable. In addition, the change of size is low due to the low optical power achieved in this lens. As mentioned above, these parameters could be enhanced with other LC mixtures and optimization of the applied voltages.

Finally, the switching time of LC devices depends mainly on the device thickness, being quadratically proportional to it. In this case, the devices are relatively thick (around 80 μm), for this reason, the switching times are around 25 seconds. Hence, this device is not intended for fast switching lenses. However, the switching speed can be improved by using nematic LC with higher anisotropy and/or lower viscosity. Moreover, it is possible to improve the device speed by using multi-stack configurations or polarization controlled stacks, such that millisecond responses could be achieved.

Optics EXPRESS

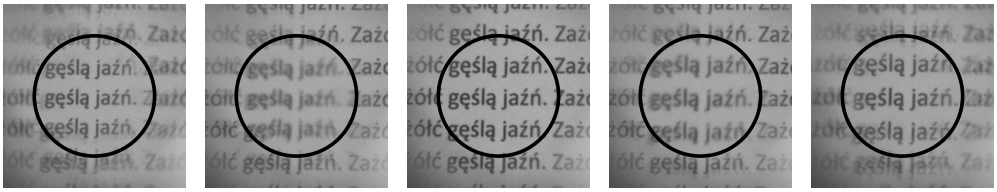

Fig. 6. Different images of the lens performance (a) V_1= 1.4 V_{RMS} and V_2 = 4.5 V_{RMS} focused. (b) V_1= 1.4 V_{RMS} and V_2 = 4.5 V_{RMS}. (c) Lens switched off. (d) V_1= 1.85 V_{RMS} and V_2 = 0.6 V_{RMS}. (e) V_1= 1.85 V_{RMS} and V_2 = 0.6 V_{RMS} focused.

4. Conclusions

In this work, a novel technique to create aspherical liquid crystal lenses is proposed and experimentally demonstrated. The main key advantages over previous methods are the simple fabrication process (one lithographic step) and the simple voltage control. As it is demonstrated, the phase shift can be controlled with voltages from 0 to 4.5 V_{RMS}. Furthermore, parabolic profiles are obtained both for negative and positive optical powers. In conclusion, this solution is easy to design, fabricate and escalate. Moreover, the shape of the phase profiles can be modified by selecting the transmission electrode parameters, allowing for the control of different aberrations. For these reasons, this novel LC lens could open new avenues of research in several applications, from ophthalmology to virtual and augmented reality displays, in which tunable aspherical phase profiles could provide advanced functionalities.

Funding. Wojskowa Akademia Techniczna (UGB 22-791); Ministerio de Ciencia, Innovación y Universidades (Juan de la Cierva Incorporación); European Social Fund (NAWA PROM projekt nr POWR.03.03.00-00-PN13/18); Comunidad de Madrid and FEDER Program (S2018/NMT-4326); MCIN/ AEI/10.13039/501100011033 and European Union "Next generation EU"/PTR (PDC2021-121172-C21); MCIN/ AEI/10.13039/501100011033 and FEDER "A way to make Europe" (PID2019-107270RB-C21, PID2019-109072RB-C31, RTC-2017-6321-1).

Disclosures. The authors declare no conflicts of interest.

Data availability. Data underlying the results presented in this paper are not publicly available at this time but may be obtained from the authors upon reasonable request.

References

1. A. Schenning, G. P. Crawford, and D. J. Broer, *Liquid crystal sensors* (CRC Press, 2017).
2. J. F. Algorri, P. C. Lallana, V. Urruchi, and J. M. Sánchez-Pena, "Liquid crystal temperature sensor based on three electrodes and a high resistivity layer," IEEE Sensors J. **15**(9), 5222–5227 (2015).
3. C. Vázquez Garcìa, I. Pérez Garcilópez, P. Contreras Lallana, B. Vinouze, and B. Fracasso, "Liquid crystal optical switches," in *Optical Switches*, (Elsevier, 2010), pp. 206–240.
4. R. Davies and M. Kasper, "Adaptive Optics for Astronomy," Annu. Rev. Astron. Astrophys. **50**(1), 305–351 (2012).
5. L. Hu, L. Xuan, Z. Cao, Q. Mu, Z. Peng, Y. Liu, L. Yao, C. Yang, X. Lu, and D. L. M. Xia, "The state of the art for liquid crystal adaptive optics in astronomical applications," in *2012 International Conference on Optoelectronics and Microelectronics*, (IEEE, 2012), pp. 428–430.
6. D. C. Zografopoulos and R. Beccherelli, "Plasmonic Variable Optical Attenuator Based on Liquid-Crystal Tunable Stripe Waveguides," Plasmonics **8**(2), 599–604 (2013).
7. D. C. Zografopoulos, R. Beccherelli, A. C. Tasolamprou, and E. E. Kriezis, "Liquid-crystal tunable waveguides for integrated plasmonic components," Photonics Nanostructures – Fundamentals Appl. **11**(1), 73–84 (2013).
8. J. M. Otón, E. Otón, X. Quintana, and M. A. Geday, "Liquid-crystal phase-only devices," J. Mol. Liq. **267**, 469–483 (2018).
9. J. F. Algorri, V. Urruchi, N. Bennis, J. M. Sánchez-Pena, and J. M. Otón, "Tunable liquid crystal cylindrical micro-optical array for aberration compensation," Opt. Express **23**(11), 13899–13915 (2015).
10. H.-S. Chen, Y.-J. Wang, C.-M. Chang, and Y.-H. Lin, "A Polarizer-Free Liquid Crystal Lens Exploiting an Embedded-Multilayered Structure," IEEE Photonics Technol. Lett. **27**(8), 899–902 (2015).
11. Y.-H. Lin, M.-S. Chen, and H.-C. Lin, "An electrically tunable optical zoom system using two composite liquid crystal lenses with a large zoom ratio," Opt. Express **19**(5), 4714 (2011).

Optics EXPRESS

12. E. Oton, P. Morawiak, R. Mazur, X. Quintana, M. A. Geday, J. M. Oton, and W. Piecek, "Diffractive and Refractive Liquid Crystal Devices Based on Multilayer Matrices," J. Lightwave Technol. **37**(9), 2086–2093 (2019).
13. H. Li, J. Peng, F. Pan, Y. Wu, Y. Zhang, and X. Xie, "Focal stack camera in all-in-focus imaging via an electrically tunable liquid crystal lens doped with multi-walled carbon nanotubes," Opt. Express **26**(10), 12441 (2018).
14. J. F. Algorri, V. Urruchi, N. Bennis, and J. SáSchenningnchez-Pena, "Cylindrical liquid crystal microlens array with rotary optical power and tunable focal length," IEEE Electron Device Lett. **36**(6), 582–584 (2015).
15. J. F. Algorri, V. Urruchi, B. Garcia-Camara, and J. M. Sanchez-Pena, "Generation of Optical Vortices by an Ideal Liquid Crystal Spiral Phase Plate," IEEE Electron Device Lett. **35**(8), 856–858 (2014).
16. M. Ca no-García, X. Quintana, J. M. Otón, and M. A. Geday, "Dynamic multilevel spiral phase plate generator," Sci. Rep. **8**(1), 15804 (2018).
17. S. P. Kotova, A. M. Mayorova, and S. A. Samagin, "Formation of ring-shaped light fields with orbital angular momentum using a modal type liquid crystal spatial modulator," J. Opt. **20**(5), 055604 (2018).
18. D. W. Berreman, "Variable-focus LC-lens system," U.S. patent US4190330A(26 February 1980).
19. S. Sato, "Liquid-Crystal lens-cell with variable focal length," Jpn. J. Appl. Phys. **18**(9), 1679–1684 (1979).
20. S. T. Kowel and D. S. Cleverly, "A Liquid Crystal Adaptive Lens," in *NASA Conference on Optical Information Processing for Aerospace Applications*, (Virginia, USA, 1981).
21. M. A. Geday, M. Ca no-García, J. M. Otón, and X. Quintana, "Adaptive Spiral Diffractive Lenses-Lenses With a Twist," Adv. Opt. Mater. **8**(23), 2001199 (2020).
22. J. Beeckman, T.-H. Yang, I. Nys, J. P. George, T.-H. Lin, and K. Neyts, "Multi-electrode tunable liquid crystal lenses with one lithography step," Opt. Lett. **43**(2), 271 (2018).
23. L. Li, D. Bryant, and P. J. Bos, "Liquid crystal lens with concentric electrodes and inter-electrode resistors," Liq. Cryst. Rev. **2**(2), 130–154 (2014).
24. Y.-Y. Kao, P. C.-P. Chao, and C.-W. Hsueh, "A new low-voltage-driven GRIN liquid crystal lens with multiple ring electrodes in unequal widths," Opt. Express **18**(18), 18506 (2010).
25. E. G. Abramochkin, A. A. Vasiliev, P. V. Vashurin, L. I. Zhmurova, V. A. Ignatov, and A. F. Naumov, "Controlled liquid crystal lens," preprint of P. N. Lebedev Phys. Inst. **194**, 18 (1988).
26. A. F. Naumov, M. Y. Loktev, I. R. Guralnik, and G. V. Vdovin, "Liquid-crystal adaptive lenses with modal control," Opt. Lett. **23**(13), 992–994 (1998).
27. G. D. Love and A. F. Naumov, "Modal liquid crystal lenses," Liquid Crystals Today **10**(1), 1–4 (2000).
28. N. Fraval and J. L. de Bougrenet, "Low aberrations symmetrical adaptive modal liquid crystal lens with short focal lengths," Appl. Opt. **49**(15), 2778–2783 (2010).
29. T. V. Galstian, *Smart Mini-Camera* (CRC Press, 2013).
30. T. Galstian, O. Sova, K. Asatryan, V. Presniakov, A. Zohrabyan, and M. Evensen, "Optical camera with liquid crystal autofocus lens," Opt. Express **25**(24), 29945 (2017).
31. T. Galstian, K. Asatryan, V. Presniakov, and A. Zohrabyan, "Electrically variable liquid crystal lenses for ophthalmic distance accommodation," Opt. Express **27**(13), 18803–18817 (2019).
32. Creative Technology Ltd., "Creative Live! Cam Connect HD," https://support.creative.com/Products/ProductDetails.aspx?prodID=20986.
33. Karbonn, "Titanium S35 model, c.J," https://www.devicespecifications.com/en/model/3ac03664.
34. J. F. Algorri, D. C. Zografopoulos, V. Urruchi, and J. M. Sánchez-Pena, "Recent Advances in Adaptive Liquid Crystal Lenses," Crystals **9**(5), 272 (2019).
35. Y.-H. Lin, Y.-J. Wang, and V. Reshetnyak, "Liquid crystal lenses with tunable focal length," Liq. Cryst. Rev. **5**(2), 111–143 (2017).
36. J. F. Algorri, P. Morawiak, N. Bennis, D. C. Zografopoulos, V. Urruchi, L. Rodríguez-Cobo, L. R. Jaroszewicz, J. M. Sánchez-Pena, and J. M. López-Higuera, "Positive-negative tunable liquid crystal lenses based on a microstructured transmission line," Sci. Rep. **10**(1), 10153 (2020).
37. J. F. Algorri, P. Morawiak, D. C. Zografopoulos, N. Bennis, A. Spadlo, L. Rodriguez-Cobo, L. R. Jaroszewicz, J. M. Sanchez-Pena, and J. M. Lopez-Higuera, "Cylindrical and Powell liquid crystal lenses with positive-negative optical power," IEEE Photonics Technol. Lett. **32**(17), 1057–1060 (2020).
38. J. F. Algorri, D. Zografopoulos, A. Spadlo, L. Rodríguez-cobo, L. R. Jaroszewicz, J. M. Sánchez-pena, and J. M. López-Higuera, "Multifunctional light beam control device by stimuli-responsive liquid crystal micro-grating structures," Sci. Rep. **10**, 1–10 (2020).
39. J. F. Algorri, D. C. Zografopoulos, L. Rodríguez-Cobo, J. M. Sánchez-Pena, and J. M. López-Higuera, "Engineering Aspheric Liquid Crystal Lenses by Using the Transmission Electrode Technique," Crystals **10**, 835 (2020).
40. C. Anthes, R. J. García-Hernández, M. Wiedemann, and D. Kranzlmüller, "State of the art of virtual reality technology," *IEEE Aerospace Conference Proceedings* **2016-June** (2016).
41. T. Ueno and Y. Takaki, "Super multi-view near-eye display to solve vergence-accommodation conflict," Opt. Express **26**(23), 30703–30715 (2018).
42. Y.-J. Wang and Y.-H. Lin, "Liquid crystal technology for vergence-accommodation conflicts in augmented reality and virtual reality systems: a review," Liq. Cryst. Rev. **9**(1), 35–64 (2021).
43. C. Pruss, E. Garbusi, and W. Osten, "Testing aspheres," Opt. Photon. News **19**(4), 24–29 (2008).
44. R. Dabrowski, J. Dziaduszek, and T. Szczucinski, "4-/Trans-4'-n-Alkylcyclohexzyl/Isothiocyanatobenzenes a New Class Of Low-Melting Stable Nematics," Mol. Cryst. Liq. Cryst. **102**(5), 155–160 (1984).

Optics EXPRESS

45. J. F. Algorri, V. Urruchi Del Pozo, P. Pinzón, and J. M. Sánchez Pena, "Modeling electro-optical response of nematic liquid crystals by numerical methods," Opt. Pura Apl. **46**(4), 327–336 (2013).
46. J.-J. Gao, J.-W. Pan, J.-W. Pan, S.-C. Jeng, and S.-C. Jeng, "Low-aberration liquid crystal lens with positive and negative focal length," Opt. Lett. **45**(18), 5077–5080 (2020).

163.117.139.147 {ts '2023-04-12 07:07:25'}